Research in Astronomy and Astrophysics, 22:085005 (11pp), 2022 August https://doi.org/10.1088/1674-4527/ac7129

Analyzing Dominant 13.5 and 27 day Periods of Solar Terrestrial Interaction: A New Insight into Solar Cycle Activities

Rissnalin Syiemlieh[1], Manashee Adhikary[1,2], Prasanta K Panigrahi[3], and Eeshankur Saikia[1]
[1] Department of Applied Sciences, Gauhati University, Assam 781 014, India; eeshankur.gu@gmail.com
[2] Complex Photonic Systems, MESA+ Institute for Nanotechnology, University of Twente, P.O. Box 217, 7500 AE Enschede, The Netherlands
[3] Department of Physical Sciences, Indian Institute of Science Education and Research, Kolkata 741 246, India
Received 2022 February 16; revised 2022 April 12; accepted 2022 April 29; published 2022 July 15

Abstract

Our analysis presents an explanation of the Sun–Earth coupling mechanism during declining phase of a solar cycle, and how the dominant 13.5 and 27 day periods play roles in the coupling mechanism which led to intense terrestrial magnetic storms during this declining phase compared to the rising phase of a solar cycle. Moreover, it is observed that while the 27 day period gets strongly modulated in the rising phase, the 13.5 day period modulation is more prominent during the declining phase. It is suggested that out of the 27 and 13.5 day periods of Sun–Earth interaction, the preferred period of modulation happens to be the one which is more dominant for the less random or quieter system participating in the coupling. It is reported for the first time that the 13.5 day period is more prominent in the Sun–Earth interaction during the declining phase of a solar cycle, as it is the most dominant period of Earth's magnetic system, which happens to be more persistent as a dynamical system and hence quieter or more receptive than the Sun.

Key words: (Sun:) solar wind – (Sun:) sunspots – (Sun:) solar-terrestrial relation – (Sun:) activity – methods: data analysis

1. Introduction

It is a known fact that solar activity influences space weather and other geomagnetic phenomenon which indeed are important as they mostly lead to geomagnetic storms (Kane 1976; Zhang & Moldwin 2014; Runge et al. 2018). They have a strong impact on hemispheric and geomagnetic disturbances due to their transient activities (Richardson et al. 2000; Zhang et al. 2006, 2007; Zhang & Moldwin 2014; Katsavrias et al. 2016; Runge et al. 2018). As observed by Kepko et al. (2002), oscillation in the magnetosphere is directly driven by density oscillation of solar wind (SW). Plasma's speed, temperature and density are the measured variables of SW which indirectly quantify activity on the surface of the Sun. Therefore, solar activity and their interaction are indeed an area of interest. Donnelly & Puga (1990) explained the existence of the 13 day period which is due to the two solar stream events per solar rotation, produced by the solar rotational modulation from two groups of active regions roughly 180 degrees apart in solar longitude. Chowdhury et al. (2013) reported the evolution periods of the photospheric magnetic-field are 26 and 13.5 days, providing a connection between the sub-photospheric magnetic field evolution, coronal activity and the loss of magnetic flux through coronal X-ray emission. Xie et al. (2017) did a detailed analysis on the solar mean magnetic field for rotational period, where the existence of the 27 and 13.5 day periods on their temporal variation was reported. They also studied the dependence of the length of rotational cycle on solar cycle phase, and suggested that there was an indication of longer rotational cycle length during the rising phase of the solar cycles in comparison to the declining phase. In the work of Le et al. (2013), it was reported that the probability of occurrence of storms is more prominent two years before and three years after a solar maximum. The study found that the probability of occurrence of geomagnetic storms during the rising phase was 27%, whereas that during the declining phase of a solar cycle was 73%. It is well accepted that the declining phase has a higher probability of occurrence of geomagnetic storms, compared to the rising phase of a solar cycle (Mursula & Zieger 1996; Emery et al. 2011; Le et al. 2013; Chowdhury et al. 2015; Mursula et al. 2015), and that there exists the dominant 13.5 day period during which the SW particles interact with Earth's geomagnetic field (GMF) (Mursula & Zieger 1996; Sanalkumaran Nair 2002; Katsavrias et al. 2012), though the reason behind this important phenomenon and dominance of the 13.5 day period during the interaction is still awaiting explanation.

The main motivation of this work is to analyze the time series of different direct and derived parameters of SW, interplanetary magnetic field (IMF) and GMF, spread over four solar cycles which are solar cycles 21, 22, 23 and 24, as an effort to contribute toward a better understanding of the solar-terrestrial coupling and try to answer the question which arises as to why geomagnetic storms are seen more in the declining half of solar cycles? We propose the analysis in two steps: first, we must examine and confirm that the declining half of a solar cycle must have more activity in comparison to the rising half of that cycle. Second, we try to give an explanation as to why and for what reason this is happening. Now, we start by dividing the data into two phases, one being the phase when the Sun moves from minima to maxima and the other is when it shifts from maxima to minima, taking the solar maximum as the reference point for each solar cycle considered. Before applying the statistical tools of data analysis, the peaks as seen in the time series are tallied with the solar images in order to ensure that the periodicities estimated are real, and not due to artifacts.

2. Data

Data are acquired from the OMNIWeb database (King & Papitashvili 2003), with daily average resolution for four solar cycles, spread over 42 yr. The database consists of a data set from different spacecraft used at 1 au. We extracted the relevant time series data of magnetic field and plasma speed in SW, solar activity indices and parameters from the GMF as well as IMF (King & Papitashvili 2005).

Parameters chosen to analyze are SW plasma's temperature, density and speed, varying with solar latitude and longitude over time. The scalar and vector forms of IMF averages, IMF's components B_x, B_y, B_z measured in the Geocentric Solar Ecliptic (GSE) and Geocentric Solar Magnetic (GSM) coordinates. The plasma flow pressure is known as ram pressure. These components bear the signature of SW plasma, also referred to as heliospheric magnetic field, dragged out from the solar corona to fill the solar system. F10.7-index is an hourly solar radio flux measure, which is the noise level generated by the Sun's activity at wavelength 10.7 cm. Sunspot number, or SSN (R_Z), is an hourly observation of the sunspot counts appearing on the solar surface.

The geomagnetic field indices (GMIs) measure the Earth's magnetic disturbances caused by the external transient phenomenon. While the ap-index measures the general level of geomagnetic activity, the Kp-index measures the horizontal disturbance component of Earth's magnetic field. Both these indices are measured at an interval of 3 hr. The Disturbance Storm Time (Dst) index measures the geomagnetic activity to gauge the severity of a magnetic storm. AE-index is the measure of geomagnetic disturbance from the auroral electrojets quantifying the strength of the disturbed period caused in the process of increasing and expanding to higher/lower latitudes, instead of confining itself to the auroral oval. The AE-index is also defined by the separation between the upper and lower envelopes of the superposed horizontal component of the auroral zone in magnetic observatories. AE = AU − AL, where AU is the upper horizontal component and AL is the lower horizontal component of AE. Polar Cap (PC) index which is a measure of single surface geomagnetic disturbance at the polar region. Dst-, AE- and PC-indices are measured at an hourly interval (Kane 1976; Chowdhury et al. 2015). To ensure that all possible aspects of multifactorial correlation are taken into consideration while analyzing in the conventional procedure, only R_Z, ap-index and SW plasma speed are used.

The Solar and Heliospheric Observatory (SOHO) (SOHO 2020) is utilized to study the Sun from its deep core to the outer corona and SW. Its database provides Large Angle and Spectrometric Coronograph (LASCO) C2 and C3 images of the solar corona. The coronal streamers are most prominent in these images. C2 images show the inner solar corona and C3 images reveal the solar corona with large distance covered away from the Sun. The LASCO C2 images are acquired for our purpose (SOHO 2020). These coronagraphic behaviors of the Sun are combined with the time series under study to ensure the absence of any artifact. For simplicity, LASCO C2 images and the original R_Z time series of 90 days (2003 January 1 to March 31) are extracted. These are combined to make sure the time periods estimated, and other inferences that are drawn from them later, match the variations observed in the solar images, negating the possibility of incorporating artifact-induced periodicities in the analysis (Song & Russell 1999).

3. Methods and Results

3.1. Time Series Analysis

Figure 1 displays the time series plots of GMIs (Kp-index, ap-index, Dst-index and pc-index), SW (SW plasma speed) and IMF (B_z(GSE)) from 2003 January 1 to March 31 (SC 23 declining phase), covering three solar rotations, plotted to check the possibility of finding the 13.5 and 27 day periods, even before statistical tools are employed for the analysis. After cleaning the time series, the missing values are taken care of by applying interpolation (Zeileis et al. 2014). Peaks are marked to assess the periodicity. Next the outliers present in the time series are removed and the previous step is repeated. Lastly, moving average (MA) (Hyndman et al. 2020) is also employed to ensure appropriate identification of the peaks. While the 13.5 day period peaks are marked by a, b, c, d, etc., the 27 day period is denoted by 1, 2, 3, etc. in the time series plot featured in Figure 1. Further, in order to verify the periods estimated from the truncated time series, the LASCO C2 images, as depicted in Figure 2, are extracted for those days when the peaks are observed from the time series.

3.2. Power Spectral Analysis

Fourier analysis conducted shows that there is significant increase in the Fourier power of all the periods, of our interest, in the declining phase. A few of these plots are provided as supporting information (SI) for reference (Figures 1, 2 and 3 in SI). This hints at, and also shows up in our analysis, gradual acceleration of solar activities, in the form of coronal holes, coronal mass ejection (CME), solar flare, etc., starting from the

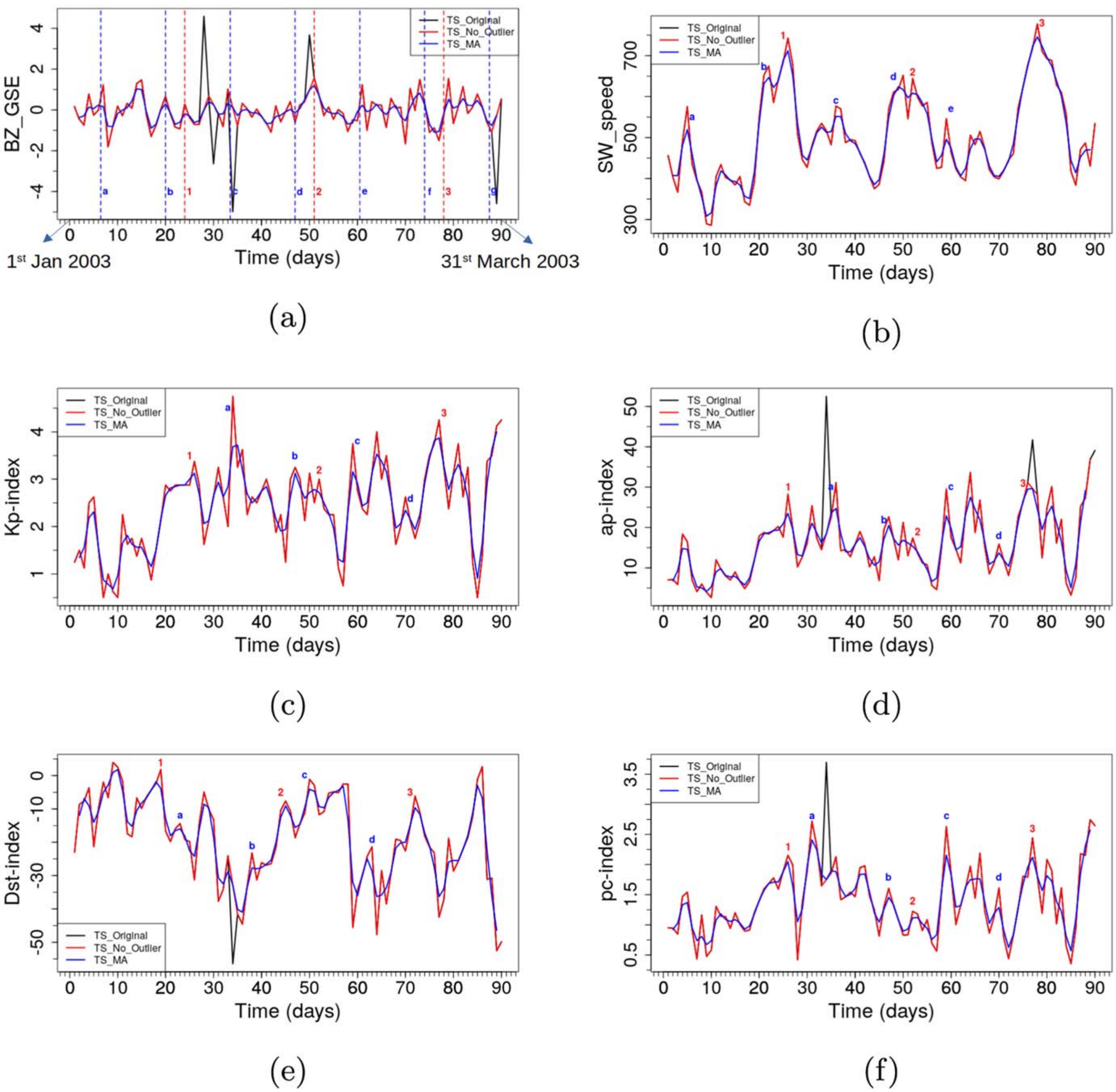

Figure 1. Plots of IMF, SW and GMI time series for 90 days during the declining phase of solar cycle 23 (ranging from 2003 January 1 to March 31), along with the MA, and cleaned (without the outliers) series. The 13.5 day ($a - b \approx b - c \approx c - d \approx d - e \approx e - f \approx f - g \approx 13.5$ day) and 27 day ($1 - 2 \approx 2 - 3 \approx 27$ day) periods are observed in all the time series.

rising phase and becoming more prominent during the declining phase. Thus, this leads to high speed streams of SW during solar maxima which continues throughout the declining phase, as also reported by Zirker (1977).

Wavelet transformation, as described by Torrence and Compo (Torrence & Compo 1998; Mallat 2008; Addison 2016), is performed using Morlet wavelets to check for periods and their strengths (De Moortel & McAteer 2004; Liu et al. 2007). The mathematical expression of a Morlet wavelet implemented in our analysis is

$$\psi(t) = \pi^{-1/4} e^{i\omega t} e^{-t^2/2}, \tag{1}$$

with angular frequency (ω) set to 6, since it makes the Morlet wavelet approximately analytic and is the preferred value in

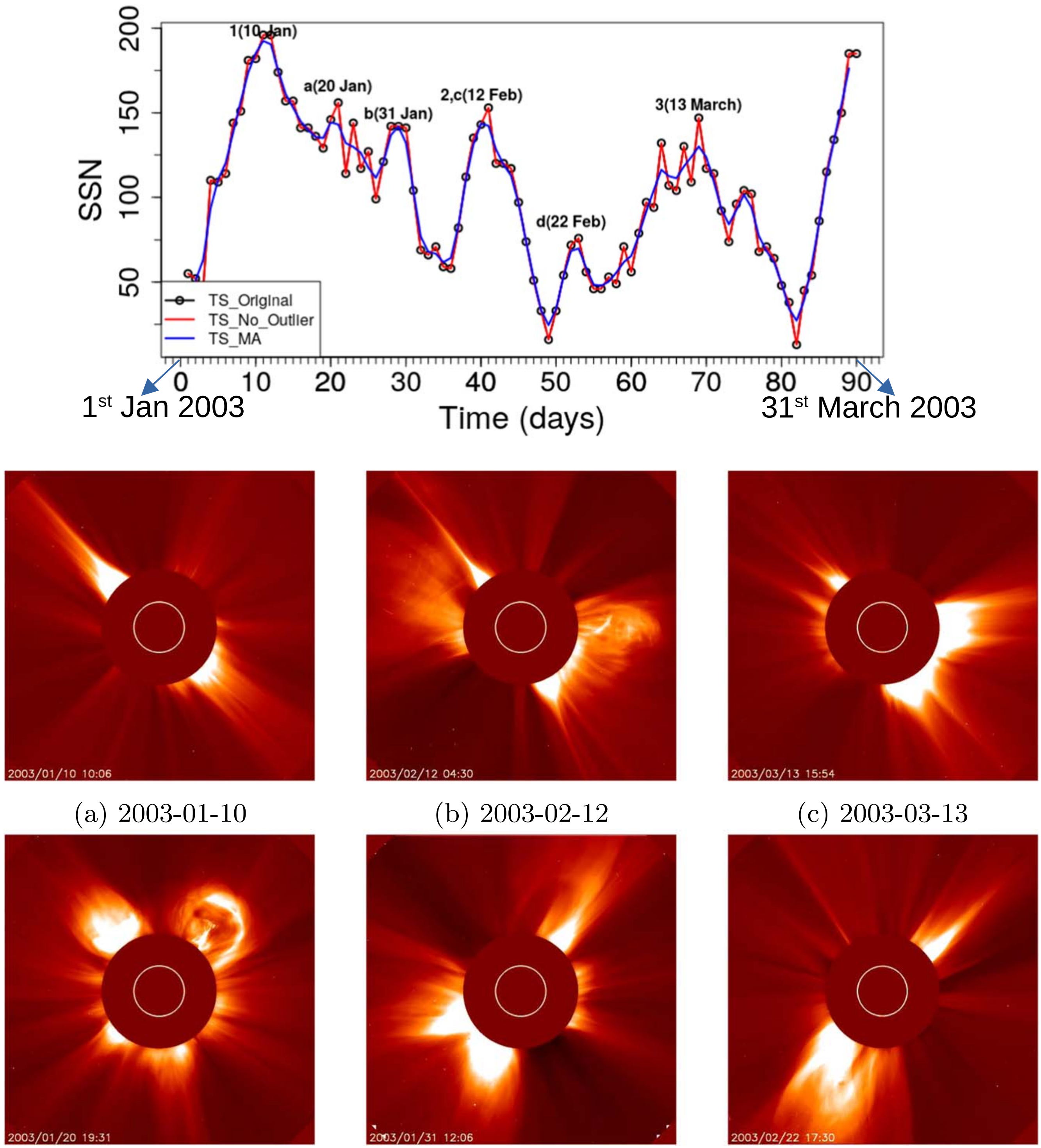

(a) 2003-01-10 (b) 2003-02-12 (c) 2003-03-13

(d) 2003-01-20 (e) 2003-01-31 (f) 2003-02-22

Figure 2. The plot displays the time series of SSN from 2003 January 1 to March 31, and below are LASCO C2 images (obtained from SOHO) of the 10th, 20th, 31st days of January 2003; 12th, 22nd days of February 2003 and the 13th day of March 2003, matching the observed time series peaks. The subfigures (a), (b) and (c), indicating the CMEs of peaks 1, 2 and 3 in the time series, verify the presence of a 27 day period; and the subfigures (d), (e), (b) and (f), indicating the CMEs of peaks a, b, c and d in the time series, correspond to a 13.5 day period.

literature (Morlet et al. 1982a, 1982b; Farge 1992; Roesch & Schmidbauer 2018). The wavelet scalogram of the variables clearly shows that the periods observed during Fourier analysis are also observed in the continuous wavelet transform (CWT) power spectrum. Almost all variables manifest a continuous distribution of higher wavelet power throughout the declining phase in each solar cycle, highlighting the importance of the declining phase for intercorrelation of the SW, IMF and GMI.

3.3. Correlation Analysis

Statistical correlation analysis suggests that there is significantly high correlation between SW plasma speed and GMIs (Kp-index and ap-index) for all the four solar cycles considered. To understand their correlation and interaction in detail, we perform cross wavelet transform (XWT) (Foufoula-Georgiou & Kumar 1994; Carmona et al. 1998; Torrence & Compo 1998; Liu et al. 2007; Veleda et al. 2012; Roesch & Schmidbauer 2018). The XWT analysis uses Morlet-wave and white noise processes for producing the correlation plots. We observe from the high average coherence value in both the phases of a cycle (Figure 3) that the 27 day period, the rotational period of the Sun, is preferred more than others for the Sun–Earth interaction. Figure 3(e) and (f) shows the cross-wavelet coherence of the two time series of R_z and ap-index, indicating significant correlation between these variables, having phase locking over time. The arrows in Figure 3(a), (b), (e) and (f) suggest that there is a phase-mixing in case of 27 day period, which is evident from their random orientation. Also, the 13.5 day period, which is seen to have less significant average coherence value in the rising phase, significantly increases its average coherence value in the declining phase. This confirms that the 13.5 day period is modulated more in the declining phase in comparison to the rising phase. Furthermore, Figure 4, which shows the average cross-wavelet power of the SW with GMI, also confirms stronger modulation of the 13.5 day period during the declining phase.

All these three analyses reassure and confirm the results reported by Le et al. (2013). To explain the high numbers of geomagnetic storms in the declining phase of a solar cycle, we proceed with the nonlinear and fractal analysis of the time series and hence briefly discuss it in the next section.

3.4. Nonlinear Dynamical and Fractal Dimension Analysis

In order to quantify and analyze the inherent nonlinearity in any two interacting dynamical systems, the rescaled range (R/S) method is used to find the Hurst exponent (H) which quantifies the statistical dependency of a dynamically evolving system (Mandelbrot & Wallis 1969). Here, H is determined using the slope of the linear regression (Suyal et al. 2009; Constantine & Percival 2017). The system behaves as: (i) periodic if $H = 1$, (ii) random if $H = 0.5$, (iii) persistent if $H > 0.5$ and (iv) anti-persistent if $H < 0.5$ (Suyal et al. 2009).

It is important to ascertain irregularity in the time series at the microscale level which is usually missed out. One way to do so is to find the surface roughness of that time series. Here, it is achieved by measuring the fractal dimension or box dimension. The fractal dimension (D) is estimated using the box-count method, and is defined as

$$D = \lim_{\epsilon \to 0} \frac{\log N(\epsilon)}{\log(1/\epsilon)}, \tag{2}$$

where $N(\epsilon)$ is the smallest number of cubes of width ϵ in $\mathbb{R}^d$. The box-count method estimates the fractal dimension by fitting the slope of an ordinary least squares regression of $\log N(\epsilon)$ to $\log(\epsilon)$ (Hall & Wood 1993; Chan et al. 1995; Davies & Hall 2002; Gneiting et al. 2011). Figure 5 features the H and D for all four solar cycles during the rising and declining phases of SSN and ap-index. The corresponding discussion may be found in the next section.

4. Discussion

As may be found from Figures 1 and 2, the spectrometric coronograph images of the Sun validate the proposition of existing 27 and 13.5 day periodicities estimated from the peaks observed in the time series, before applying the statistical tools for the analysis.

As mentioned above, the Fourier and wavelet analyses suggest the importance of the declining phase of a solar cycle in connection with geomagnetic phenomena. The correlation analysis suggests a stronger phase correlation of the Sun–Earth system in this phase, influencing Earth's atmosphere significantly. Also, comparing the statistical correlation coefficient of GMIs (Kp, ap, AE-indices) with SW variables in both phases, we observe a significant increase in correlation coefficient for SW plasma speed variables with GMI in the declining phase for all the four solar cycles considered. In a Sun-type variable star, convection is known to drive fluid from unstable to stable zones (Saikia et al. 2003; Komm et al. 2015). The robust interior dynamics, mainly driven by convection, emanate the cyclic magnetic flow into the heliosphere, depending on how the interior strength of the magnetic field flow varies (Howe et al. 2000; Cargill et al. 2010; Cargill & De Moortel 2011; Priest 2014; Komm et al. 2015; Song & Zhang 2016). This may be the reason behind varying dimension of the coronal holes (Zhang & Low 2005; Cargill & De Moortel 2011; Song & Zhang 2016; Cheng et al. 2017), and thus explains the dominance of fast wind (McComas et al. 2000; Richardson et al. 2000; Ballatore 2003; Owens et al. 2017) in the declining phase. Hence, energy absorption from SW plasma by the magnetosphere is at its maximum (Ballatore 2003; Mursula et al. 2015) in this phase. This is supported by the correlation coefficient estimated here between SW speed and GMIs (Dst, PC -indices) during solar cycles 22, 23 and 24. The geometrical contraction of the holes in moving from solar maxima to solar

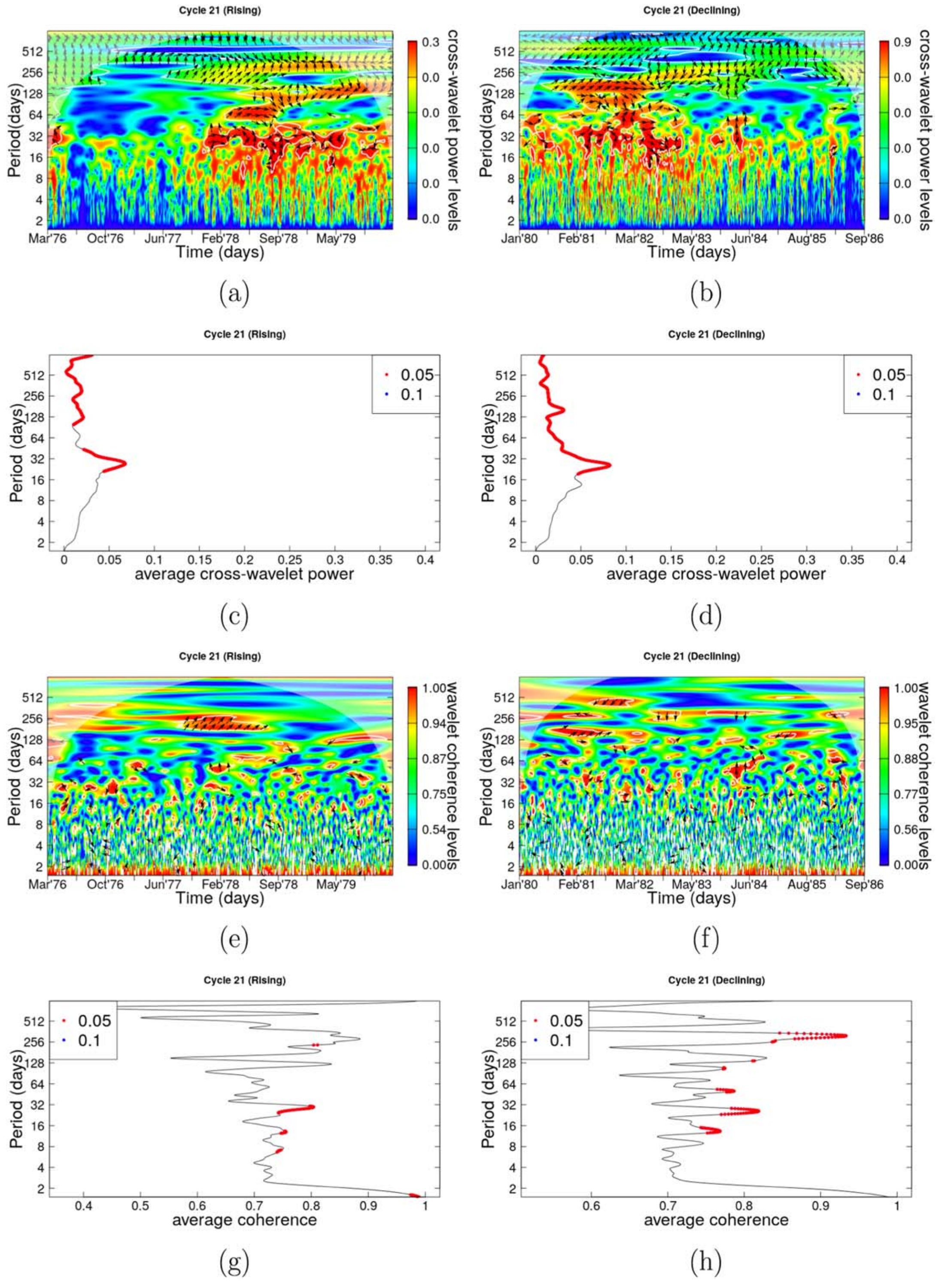

Figure 3. (a), (b) XWT power plots of GMI (ap-index) and SSN (R_z) of solar cycle 21, depicting interaction and phase behavior (marked by arrows) of Sun's activity vis-a-vis geomagnetic disturbances caused. (c), (d) Average cross-wavelet power plots showing average power value vs. periods of R_z and ap-index for solar cycle 21. The red-dots on the curve confirm 95% confidence level in the estimation. (e), (f) Wavelet coherence power plots of the Sun's activity (R_z) varying with geomagnetic disturbances (ap-index) of solar cycle 21, exhibiting significant phase mixing (marked by randomly oriented arrows) in case of 27 day period, as is also evident from (a) and (b), across time duration considered. (g), (h) Average coherence power plot of R_z and ap-index for solar cycle 21, displaying significant coherence value of all estimated periodic interactions of the two time series.

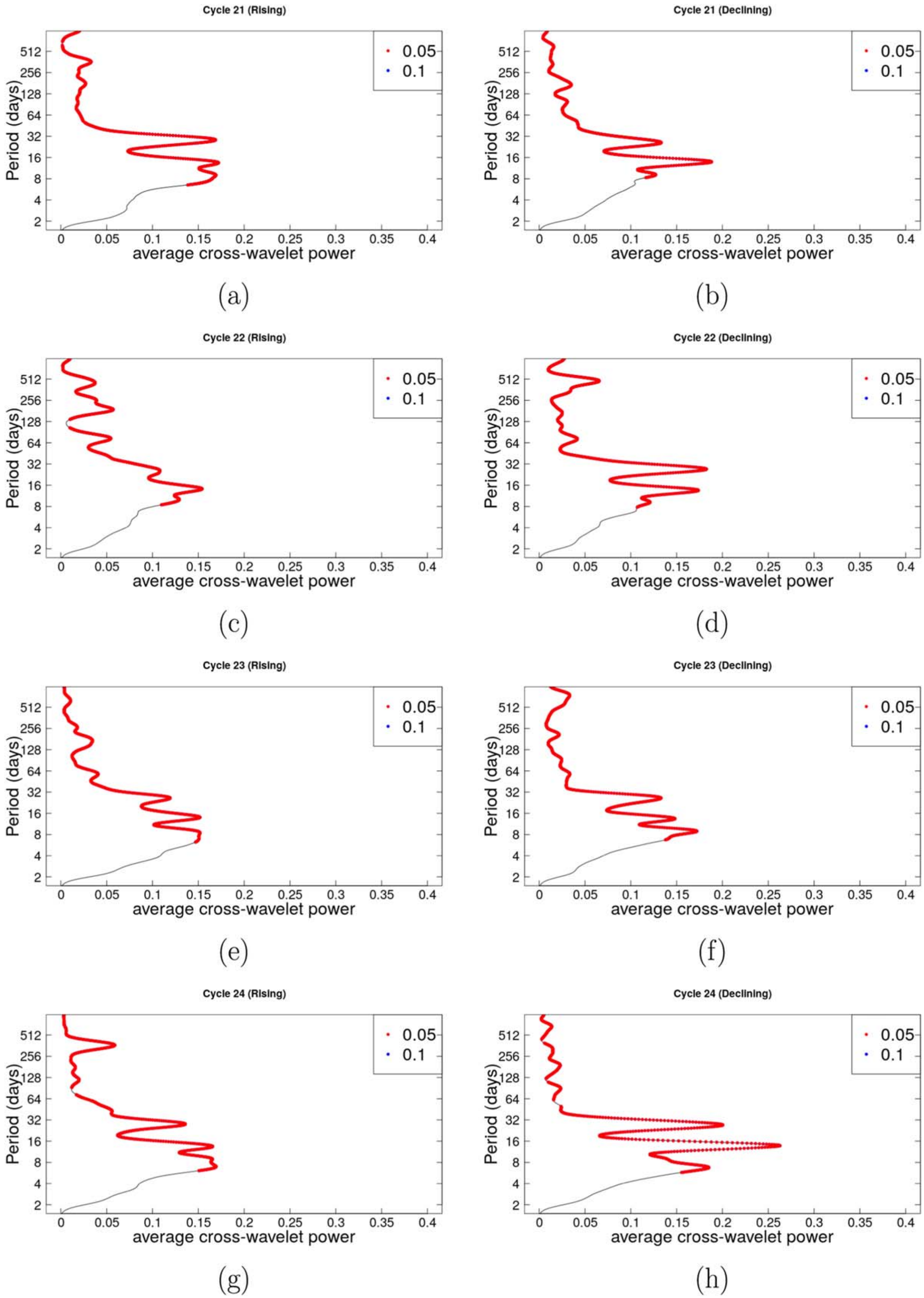

Figure 4. Average cross-wavelet power plots of SW plasma speed and GMI (ap-index).

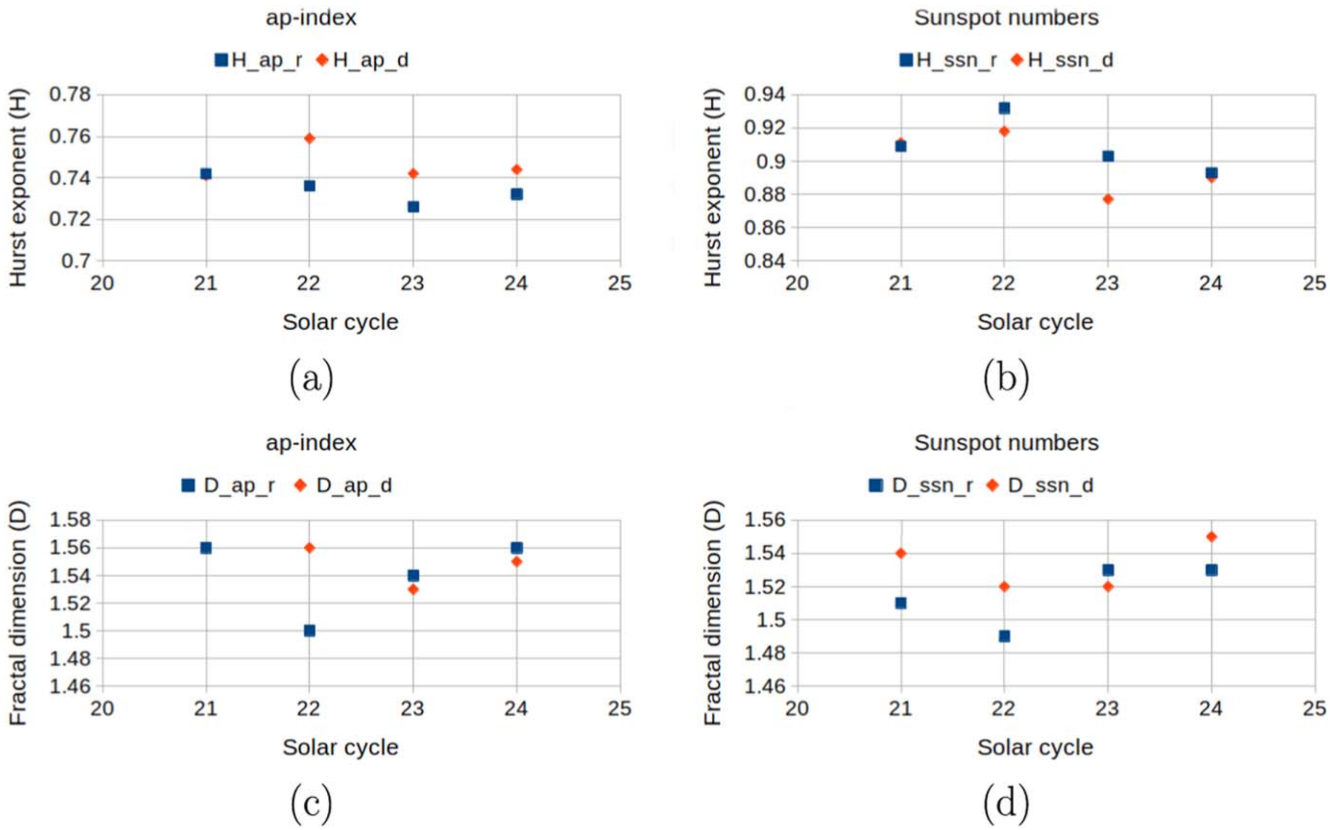

Figure 5. Results obtained: (a) Hurst exponent (*H*) estimated for ap-index during rising (*r*) and declining (*d*) phases over all the four solar cycles considered, (b) *H* estimated for SSNs, (c) fractal dimension (*D*) estimated for ap-index, and (d) *D* estimated for SSN.

minima and expansion in the reversed phase, believed to be due to the differential rotation of the Sun, explain the more prominent correlation of the Sun–Earth system during the declining phase, causing more intense SW plasma. The migration of the coronal holes from the equator to the polar region also shows an increase in the correlation between Sun–Earth at the solar maxima and declining phase of the cycle (McComas et al. 2000), indicating robust geomagnetic activity in this phase. We also observe increase in correlation of plasma flow pressure with GMIs (Dst, PC-index) for all four cycles in the declining phases. It is well known that the dynamics of SW (Guo et al. 2016) pressure disturb the magnetospheric field in Earth's magnetosphere (Kepko & Spence 2003). This causes inward flows of plasma at the magnetopause, since the balance of plasma pressure and magnetic field pressure in magnetosphere is disturbed (Verzariu et al. 1972; Sibeck & Croley 1991; Russell et al. 1992; Kepko et al. 2002; Lopez & Gonzalez 2017), increasing the tendency of geomagnetic storms during this phase of a solar cycle. The correlation coefficient of SW plasma temperature and GMI (AE-indices) also increases in the declining phase in all cycles, which explains the dynamics of the oval auroral electrojet (Chen et al. 2003; Nakamura et al. 2015). This indicates that the plasma temperature plays a major role in the expansion of the electrojet and also in the transfer of plasma energy into our atmosphere, which is also highest in this phase.

From wavelet cross-correlation and the average coherence of the Sun–Earth system, it is observed that the system is interacting more in the declining phase. The wavelet coherence and average coherence analysis of the SSN and ap-index, as mentioned above, confirm relatively stronger modulation of 27 day period during the rising phases, and of 13.5 day period modulation in declining phases of all the four solar cycles considered for the present study. We demonstrate by estimating the Hurst exponent and the fractal dimension that the Sun is quieter during the rising phase. Hence it may be confirmed from our study that as the CMEs go down during the rising phase, the 27 day period modulation too is lower during this phase, and hence the otherwise subtler 13.5 day period shows up. Except for solar cycle 21, both 13.5 and 27 day periods are more strongly modulated during the declining phase as observed in case of the average cross wavelet power between the SW plasma speed and the ap-index. The 27 day period is higher during the rising phase of cycle 21, perhaps due to the fact that it is the cycle when the rising phase is the steepest. Moreover, it appears from our analysis that except in cycle 22,

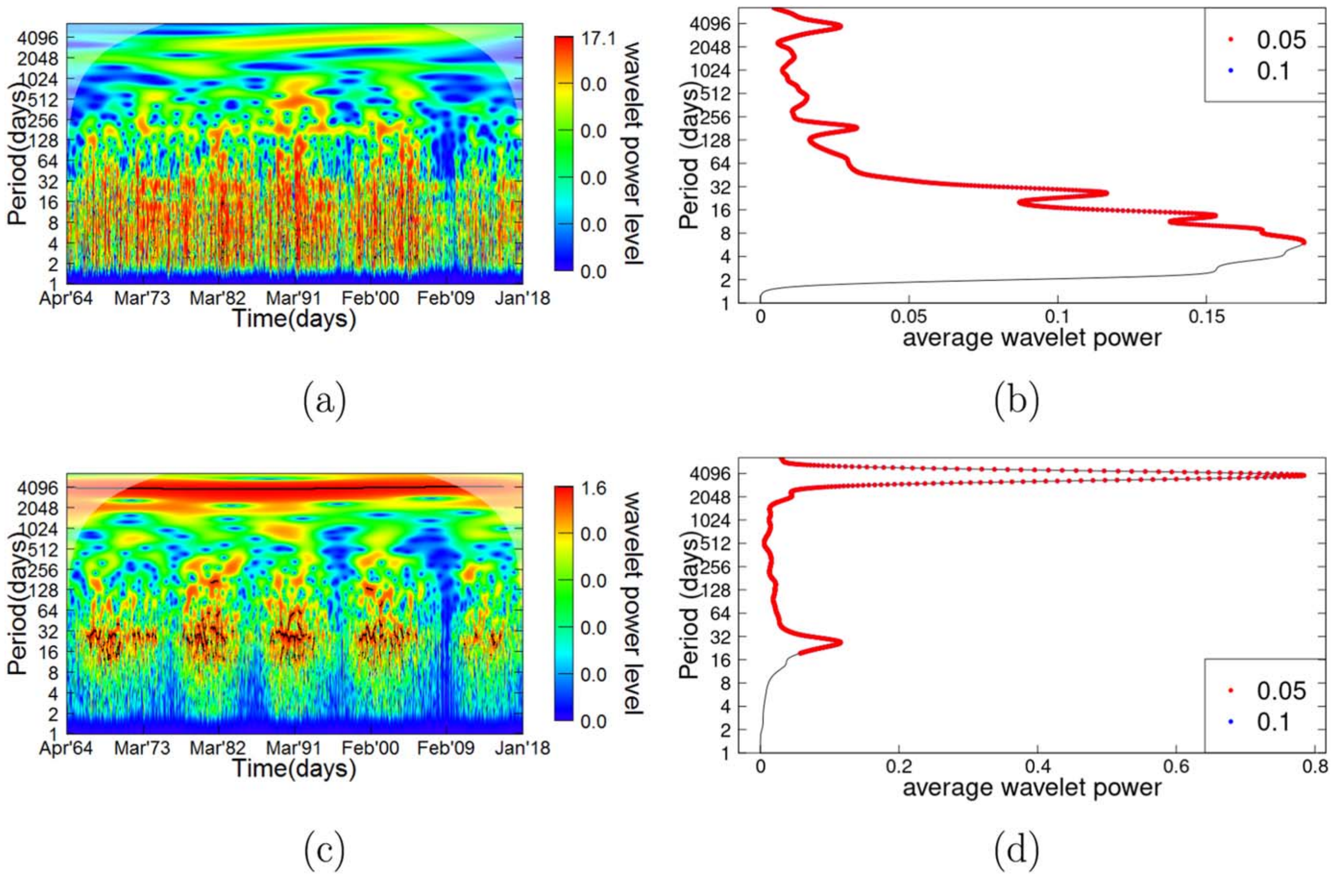

Figure 6. (a) Continuous wavelet power of ap-index (GMI) for five solar cycles, (b) average wavelet plot of ap-index, (c) continuous wavelet power of SSN for five solar cycles and (d) average wavelet plot of SSN.

the 13.5 day period gets modulated more robustly than the rest during the declining phase. This reiterates our first claim that while the Sun becomes quieter during the rising phase, Earth becomes quieter and hence more receptive during the declining phase. This leads to the second claim that the 13.5 day period is more preferred as the modulation frequency for the interaction of the Sun–Earth system during the declining phase of the solar cycle since the 13.5 day period appears to be the more dominant period than the 27 day period in case of the quieter Earth, as observed from the average power of the ap-index (Figure 6(b)). As may be found from Figure 6(d), besides 4096 days or 11.22 yr, the 27 day period is more dominant than the 13.5 day period in case of the Sun, which is the preferred period for interaction with Earth during the rising phase, as the Sun is quieter and more receptive. Thus, it is concluded that in case of Sun–Earth interaction, out of the 27 and 13.5 day periods, the preferred period of modulation happens to be the one which is more dominant for the quieter and more receptive partner. As is found from the cross wavelet power analysis of SW plasma speed and ap-index, the dominance of the 27 day period during cycle 22 is not only higher compared to that in the 13.5 day period, it is also enhanced by almost 90% in the declining phase in comparison to the rising phase.

It is clearly observed from Figure 5(a) and (b) that SSN is more persistent than the ap-index for all the four cycles considered, indicating that the variations in the terrestrial system are more random than those in the solar system, which are also supported by the estimates of the fractal dimension as depicted by Figure 5(c) and (d) where the dimension estimated is higher in case of ap-index than that in case of SSN for each individual cycle. It is also evident that while H is higher during the declining phase in case of ap-index, it is also so during the rising phase in case of SSN, confirming the proposition that the Earth becomes quieter and hence is more receptive during the declining phase when the Sun is relatively more random than its state during the rising phase. In connection with the anomaly seen in cycles 22 and 23 (refer to Figure 5(c) and (d)), it may be noted that there were 84 major geomagnetic storms reported during cycle 22, in comparison to around 60 during neighboring cycles (Le et al. 2013), and the duration of solar cycle 23 is found to be 12.3 yr, which is much higher than the neighboring ones. However, even with the anomalies seen, it may be observed that H estimated for the SSN is the highest and D is the lowest in the rising phase of cycle 22, implying that the corresponding dynamical system is the most persistent one. Hence it is confirmed that the Sun, in the rising phase, is more persistent and hence quieter in cycle 22 than the other three cycles considered. On the other hand, H measured for the ap-index shows that it is maximum in case of the declining phase of cycle 22, complementing the SSN and reassuring our proposition in regard to the coupling between the Sun–Earth system.

5. Conclusions

A detailed study of the above parameters showed a significant amplification of Fourier power for all variables in the declining phase, in comparison to that in the rising phase, affirming the importance of this phase for correlation study of the SW, IMF and GMI components. The increase in linear correlation coefficient of SW parameters with GMI for all four cycles considered suggests intense magnetic storms during this declining phase. XWT and its coherence plots of the Sun–Earth system suggest that a 27 day period is the preferred period for interaction between them during the rising phase, perhaps because it happens to be more dominant than the 13.5 day period in case of the Sun. Moreover, the present work also suggests that a 13.5 day period, which is more dominant than the 27 day period in case of the terrestrial system, is modulated more and hence observed to be more prominent in the Sun–Earth coupling process during the declining phase, probably due to more robust solar activities in the form of more intense CMEs and solar flares, while simultaneously having a quieter terrestrial system during the declining phase. The CWT and its average wavelet power plots for five solar cycles, starting from 1964, for ap-index and SSNs substantiate the above claim. The Hurst exponent and the fractal dimension estimated confirm that the Sun is quieter during the rising phase, while Earth is quieter and is in a more receptive mode during the declining phase of a solar cycle. Thus, it is concluded that in the Sun–Earth coupling, the most modulated period depends on the dominant periods of its quieter partner and, hence, behaves in such a way that one of the two constituent members is more robust while the other is quieter and more receptive.

Acknowledgments

The data used here are in the repositories of NASA and cited in the references. We thank Joe King and Natalia Papitashvili, NASA/SPDF, for making the data available in the public database of NASA/GSFC's Space Physics Data Facility's OMNIWeb service, and OMNI 2 data at https://omniweb.gsfc.nasa.gov/ow.html. Also, the Solar and Heliospheric Observatory (SOHO) LASCO C2 images describing the solar activity are available in archived format at https://soho.nascom.nasa.gov/data/data.html. SOHO is a project of international cooperation between ESA and NASA.

We are grateful to the anonymous reviewer for the queries raised and suggestions made, helping us to come up with a better version of the report. R.S. is thankful to MOTA for providing a fellowship under the NFST project, to IISER, Kolkata for providing all necessary support and to Sayantan Ghosh for his suggestions during this work.

References

Addison, P. S. 2016, The Illustrated Wavelet Transform Handbook: Introductory Theory and Applications in Science, Engineering, Medicine and Finance (Boca Raton, FL: CRC Press)
Ballatore, P. 2003, JGR, 108, 1387
Cargill, P., & De Moortel, I. 2011, Natur, 475, 463
Cargill, P., Parnell, C., Browning, P., De Moortel, I., & Hood, A. 2010, A&G, 51, 31
Carmona, R. R., Hwang, W.-L., & Torreésani, B. 1998, Practical Time-frequency Analysis: Gabor and Wavelet Transforms with an Implementation in S (New York: Academic), 490
Chan, G., Hall, P., & Poskitt, D. S. 1995, AnSta, 23, 1684
Chen, G.-X., Xu, W.-Y., Wei, Z.-G., Ahn, B. H., & Kamide, Y. 2003, EP&S, 55, 255
Cheng, X., Guo, Y., & Ding, M. 2017, ScChD, 60, 1383
Chowdhury, P., Choudhary, D. P., Gosain, S., & Moon, Y.-J. 2015, Ap&SS, 356, 7
Chowdhury, P., Jain, R., & Awasthi, A. K. 2013, ApJ, 778, 9
Constantine, W., & Percival, D. 2017, Package 'fractal': A Fractal Time Series Modeling and Analysis Package, https://CRAN.R-project.org/package=fractal
Davies, S., & Hall, P. 2002, Journal of the Royal Statistical Society: Series B (Statistical Methodology), 61, 3
De Moortel, I., & McAteer, R. 2004, SoPh, 223, 1
Donnelly, R., & Puga, L. 1990, SoPh, 130, 369
Emery, B. A., Richardson, I. G., Evans, D. S., Rich, F. J., & Wilson, G. R. 2011, SoPh, 274, 399
Farge, M. 1992, AnRFM, 24, 395
Foufoula-Georgiou, E., & Kumar, P. 1994, Wavelets in Geophysics (New York: Academic), 373
Gneiting, T., Ševčíková, H., & Percival, D. B. 2012, StaSc, 27, 247
Guo, J., Wei, F., Feng, X., et al. 2016, NatSR, 6, 1
Hall, P., & Wood, A. 1993, Biometrika, 80, 246
Howe, R., Christensen-Dalsgaard, J., Hill, F., et al. 2000, Sci, 287, 2456
Hyndman, R. J., Athanasopoulos, G., Bergmeir, C., et al. 2020, Package 'forecast': Forecasting Functions for Time Series and Linear Models, https://pkg.robjhyndman.com/forecast/
Kane, R. 1976, SSRv, 18, 413
Katsavrias, C., Hillaris, A., & Preka-Papadema, P. 2016, AdSpR, 57, 2234
Katsavrias, C., Preka-Papadema, P., & Moussas, X. 2012, SoPh, 280, 623
Kepko, L., & Spence, H. E. 2003, JGRA, 108, 1257
Kepko, L., Spence, H. E., & Singer, H. J. 2002, GeoRL, 29, 39
King, J., & Papitashvili, N. 2003, OMNI/OMNIWEB Data and Service (Accessed: 28 November 2018), https://omniweb.gsfc.nasa.gov/html/omni2_doc_old.html
King, J. H., & Papitashvili, N. E. 2005, JGRA, 110, 1
Komm, R., De Moortel, I., Fan, Y., Ilonidis, S., & Steiner, O. 2015, SSRv, 196, 167
Le, G. M., Cai, Z. Y., Wang, H. N., Yin, Z. Q., & Li, P. 2013, RAA, 13, 739
Liu, Y., San Liang, X., & Weisberg, R. H. 2007, JAtOT, 24, 2093
Lopez, R. E., & Gonzalez, W. D. 2017, GeoRL, 44, 2991
Mallat, S. 2008, A Wavelet Tour of Signal Processing: The Sparse Way (New York: Academic)
Mandelbrot, B. B., & Wallis, J. R. 1969, WRR, 5, 967
McComas, D. J., Barraclough, B. L., Funsten, H. O., et al. 2000, JGRA, 105, 10419
Morlet, J., Arens, G., Fourgeau, E., & Giard, D. 1982a, Geop, 47, 222
Morlet, J., Arens, G., Fourgeau, E., & Glard, D. 1982b, Geop, 47, 203
Mursula, K., Lukianova, R., & Holappa, L. 2015, ApJ, 801, 30
Mursula, K., & Zieger, B. 1996, JGRA, 101, 27077
Nakamura, M., Yoneda, A., Oda, M., & Tsubouchi, K. 2015, EP&S, 67, 153

Owens, M. J., Lockwood, M., & Riley, P. 2017, NatSR, 7, 41548
Priest, E. 2014, Magnetohydrodynamics of the Sun (Cambridge: Cambridge Univ. Press)
Richardson, I. G., Cliver, E. W., & Cane, H. V. 2000, JGRA, 105, 18203
Roesch, A., & Schmidbauer, H. 2018, Package 'WaveletComp': Computational Wavelet Analysis, https://CRAN.R-project.org/package=WaveletComp
Runge, J., Balasis, G., Daglis, I. A., Papadimitriou, C., & Donner, R. V. 2018, NatSR, 8, 16987
Russell, C. T., Ginskey, M., Petrinec, S., & Le, G. 1992, GeoRL, 19, 1227
Saikia, E., Das, M. K., Singh, H. P., Srivastava, M. P., & Chan, K. L. 2003, MNRAS, 343, 1002
Sanalkumaran Nair, V. 2002, PhD thesis, University of Kerala
Sibeck, D. G., & Croley, D. J. J. 1991, JGRA, 96, 1669
SOHO 1995, SOHO data and service (Accessed: 28 October 2019), https://soho.nascom.nasa.gov/
Song, P., & Russell, C. 1999, SSRv, 87, 387
Song, Y., & Zhang, M. 2016, ApJ, 826, 173
Suyal, V., Prasad, A., & Singh, H. P. 2009, SoPh, 260, 441
Torrence, C., & Compo, G. P. 1998, BAMS, 79, 61
Veleda, D., Montagne, R., & Araujo, M. 2012, JAtOT, 29, 1401
Verzariu, P., Sugiura, M., & Strong, I. B. 1972, P&SS, 20, 1909
Xie, J., Shi, X., & Xu, J. 2017, AJ, 153, 9
Zeileis, A., Grothendieck, G., Ryan, J. A., Andrews, F., & Zeileis, M. A. 2014, Package 'zoo': S3 Infrastructure for Regular and Irregular Time Series (Z's Ordered Observations), https://zoo.R-Forge.R-project.org/
Zhang, J., Liemohn, M. W., Kozyra, J. U., et al. 2006, JGRA, 111, 1
Zhang, J., Richardson, I. G., Webb, D. F., et al. 2007, JGRA, 112, 1
Zhang, M., & Low, B. C. 2005, ARA&A, 43, 103
Zhang, X.-Y., & Moldwin, M. B. 2014, JGRA, 119, 658
Zirker, J. 1977, RvGSP, 15, 257